

Real modes and null memory contributions in effective-one-body models

Simone Albanesi  *

*Theoretisch-Physikalisches Institut, Friedrich-Schiller-Universität Jena, 07743, Jena, Germany and
INFN sezione di Torino, Torino, 10125, Italy*

(Dated: June 30, 2025)

We introduce a novel approach to describe real-valued $m = 0$ modes from inspiral to merger and ringdown in effective-one-body models, including both oscillatory and null memory contributions. A crucial aspect of the modelization of the oscillatory part is the complexification of the real modes via a Hilbert transform. This procedure allows for an accurate description of the merger-ringdown waveform by applying standard approaches employed for the complex $m > 0$ modes, which include source-driven effects. The physical signal is then recovered by solely considering the real part. We apply this method in the extreme-mass-ratio regime, considering particle-driven linear gravitational perturbations in Schwarzschild and Kerr spacetimes. We then extend our description to spin-aligned, quasi-circular, comparable-mass binaries providing hierarchical fits incorporating the test-mass limit. The post-merger waveform is then matched with an inspiral effective-one-body waveform. By adopting `TEOBResumS-GIOTTO` as our baseline, we also include the displacement memory in the $(2,0)$ mode through Bondi–van der Burg–Metzner–Sachs balance laws, thus providing a complete effective-one-body model incorporating both oscillatory and null memory effects. The accuracy of this model is validated against the hybrid numerical relativity surrogate `NRHybSur3dq8_CCE`, finding, for the quadrupole of the equal mass nonspinning case, a LIGO noise-weighted mismatch of $\bar{\mathcal{F}} = 6 \times 10^{-4}$ at $50M_\odot$ for the inclination that maximizes the contribution of the $(2,0)$ mode.

Introduction – With the detections from the LIGO-Virgo-KAGRA (LVK) network [1, 2], gravitational wave (GW) astronomy has now become a standard tool for exploring the Universe [3–5]. Waveform models for compact binaries are central to this field, both for detection and data analysis, making it essential to provide accurate GW models. Moreover, the advent of next-generation detectors, such as Einstein Telescope [6, 7], LISA [8], and Cosmic Explorer [9], requires even further advancements in waveform modeling, not only in accuracy [10], but also in capturing all the physically relevant phenomena [11]. The effective-one-body (EOB) approach [15–17] is capable to accurately model GWs from compact binaries, once calibrated and complemented with numerical relativity (NR) data [18–20]. This approach does not only describe standard quasi-circular binary black holes (BBHs) [14, 21], but can be also employed to model binaries in presence of matter [22–25], eccentricity [26–34], and spin-precession [35–40], eventually jointly [41–44]. However, state-of-the-art EOB models do not include $m = 0$ modes in the co-precessing frame, despite them being particularly relevant when the radial acceleration is large, *e.g.*, on eccentric orbits or during the plunge. In this work we devise a strategy to incorporate their description, from inspiral to merger and ringdown, considering both oscillatory contributions and displacement memory effects. To build our model for the oscillatory part, we consider numerical results obtained by solving linear perturbations sourced by test-particle dynamics [45–49] with `RWZHyP` [50–52] and `Teukode` [53], together with waveforms obtained from the surrogate model `NRHybSur3dq8` [54], which is built using NR sim-

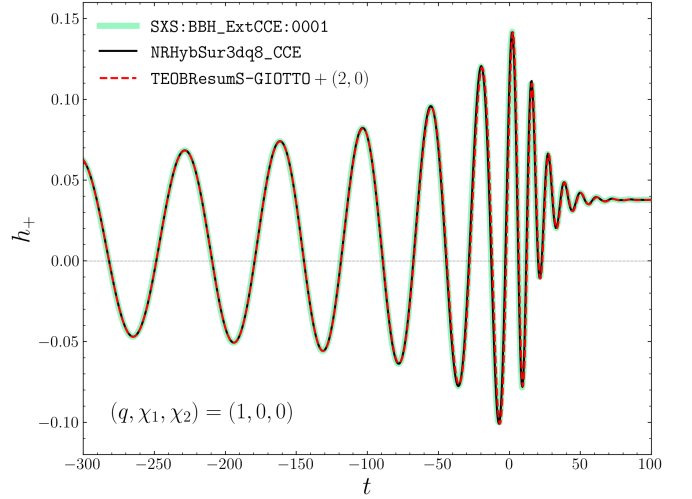


FIG. 1. Quadrupolar strains for the equal mass nonspinning case and observational direction $(\Theta, \Phi) = (\frac{\pi}{2}, 0)$. We consider the simulation `SXS:BBH_ExtCCE:0001` [12] (thick green), the surrogate `NRHybSur3dq8_CCE` [13] (solid black), and the EOB model `TEOBResumS-GIOTTO` [14] completed with the $(2,0)$ mode as discussed in this work (dashed red).

ulations of the SXS collaboration [12, 55–67]. After having discussed some phenomenological aspects, we start by extending the post-merger model of Ref. [68] to the real $m = 0$ oscillatory modes through a complexification achieved with a Hilbert transform [69, 70]. We then provide a closed-form representation of the oscillatory post-merger for the $(2,0)$ mode across the parameter space of spin-aligned binaries with generic mass ratios by means of hierarchical fits. This post-merger model is then matched with an inspiral EOB waveform based on Ref. [26], using standard next-to-quasicircular (NQC) corrections [19].

* simone.albanesi@uni-jena.de

The (2,0) mode is also sourced by the outgoing gravitational radiation, thus manifesting a nonlinear memory contribution [71–74]. This effect, which is inherently related to the radiated energy flux [72], has been studied for quasi-circular binaries in post-Newtonian (PN) theory [75, 76] and in minimal-waveform models, where an EOB inspiral/plunge waveform is completed with a post-merger model purely based on a quasi-normal-mode (QNM) description [77, 78]. Null memory contributions for eccentric inspirals have also been studied within the PN framework [79, 80] and the EOB one [81]. These effects have been resolved in NR simulations only recently [82, 83], by using Cauchy characteristic extraction (CCE) [84–88]. It should be noted that the strain, and memory effects in particular, are inherently linked to the Bondi-van der Burg-Metzner-Sachs (BMS) group [89, 90], which is the symmetry group of asymptotically flat spacetimes at future null infinity (Poincaré group plus supertranslations). Therefore, using BMS balance laws, null memory effects can also be added in post-processing to NR simulations [91, 92]. The displacement memory in the (2,0) mode has been also included in some inspiral-merger-ringdown (IMR) waveforms models [77, 78, 93], and in particular in IMRPhenomTHM [94]. Memory effects have been searched in LVK data [95, 96], and are potentially detectable with future observations [97–101].

We then apply our strategy employing **TEOBResumS-GIOTTO** [14] as a baseline, thus completing this model by including the description of the (2,0) multipole for spin-aligned quasi-circular BBHs with generic mass ratio. The oscillatory part is described with an EOB waveform completed with the aforementioned Hilbert post-merger model, while the null memory contribution is computed from BMS balance laws and matched, at low-frequencies, with the PN result [79, 80, 93]. The model is validated against the hybrid NR-surrogate **NRHybSur3dq8_CCE** [13], whose waveforms are in the same BMS frame as the EOB ones, thus avoiding any coordinate ambiguity [12, 102]. A comparison for the quadrupolar strain with this surrogate and a NR SXS simulation [12] is anticipated in Fig. 1. More details are discussed in the conclusions.

Conventions – We use geometric units $G = c = 1$. The GW strain is decomposed in multipoles on spin-weighted spherical harmonics as $h_+ - ih_\times = \sum_{\ell m} {}_{-2}Y_{\ell m}(\Theta, \Phi) R^{-1} h_{\ell m}$, being R the distance of the observer. Multipoles are further decomposed in amplitude and phase as $h_{\ell m} = A_{\ell m} e^{-i\phi_{\ell m}}$. The waveform frequency is computed as $\omega_{\ell m} = \dot{\phi}_{\ell m}$, where the dot indicates a time-derivative. If not specified otherwise, length-scales are normalized with the total rest mass of the system $M = m_1 + m_2$, where $m_{1,2}$ are the masses of the two black holes ($m_1 > m_2$). The symmetric mass ratio is defined as $\nu = q/(1+q)^2$, where $q = m_1/m_2$. The dimensionless Kerr spin is denoted as \hat{a} , with $\hat{a} \geq 0$ ($\hat{a} < 0$) for prograde (retrograde) equatorial orbits. For comparable-mass binaries, the dimensionless black hole spins are instead denoted as $\chi_{1,2}$. The time correspond-

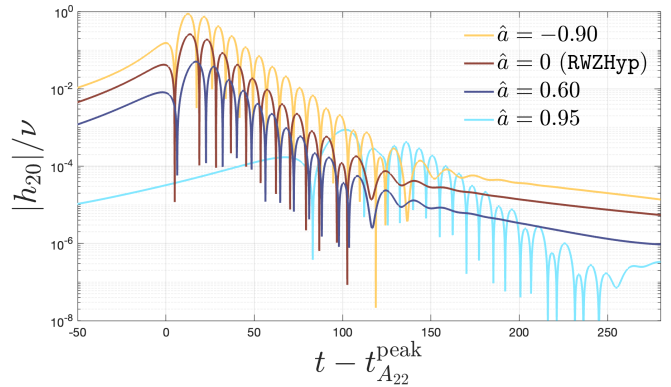


FIG. 2. (2,0) modes generated by quasi-circular evolutions in Schwarzschild and Kerr for different spin parameters \hat{a} . Aligned with respect to t_{A22}^{peak} .

ing to the peak of the (2,2) amplitude is indicated as t_{A22}^{peak} .

EOB dynamics and test-mass limit – The standard EOB approach consists in mapping the 2-body PN dynamics to the motion of a particle in an effective metric, which is a ν -deformation of the Schwarzschild or Kerr one [15–17]. The EOB Hamiltonian, together with a PN-resummed prescription for the radiation reaction, provides Hamilton’s equations that can be solved to obtain the effective dynamics, from which is then possible to analytically compute the multipolar waveform at infinity. By setting to zero the ν -corrections in the conservative sector and keeping leading-order contribution in the radiation reaction, we can evolve inspirals in Schwarzschild and Kerr spacetimes, thus obtaining a first-order description of extreme-mass ratio binaries. However, note that higher-order corrections in the mass ratio are needed to describe real astrophysical scenarios [103]. Given test-mass dynamics, we can numerically compute the linear-order gravitational perturbations sourced by the motion of the particle. This approach has been extensively used to gain insights into prescriptions to use for binaries with generic mass-ratio [19, 104–106]. In this work, we start by considering the quasi-circular inspiral of Ref. [106], obtained by solving the Regge-Wheeler and Zerilli equations with a test-particle source term [45–48] using the time-domain code **RWZHyP** [50–52]. We then explore the Kerr case, by solving the Teukolsky equation [49] for 11 quasi-circular configurations with **Teukode** [53]. The test-mass simulations are listed in Table II of the Supplemental Material (SM).

Phenomenology – In the test-mass limit, the relevance of the (2,0) mode changes substantially with the dimensionless Kerr spin \hat{a} , as shown in Fig. 2. Indeed, the (2,0) mode is enhanced for $\hat{a} < 0$, while it is suppressed for high positive spins. This can be understood by noting that the $m = 0$ multipoles are radial modes, and that the last stable orbit is larger for retrograde than for prograde orbits [107], thus leading to a more radial plunge.

Moreover, the peak of the signal is strongly delayed with respect to $t_{A_{22}}^{\text{peak}}$, as shown by the $\hat{a} = 0.95$ case. We also observe that the tail [108–110] of the $m = 0$ modes is more relevant than for $m > 0$ ones, as expected¹. Indeed, in Schwarzschild the transition from QNM to tail for the dominant mode occurs at $t \sim t_{A_{22}}^{\text{peak}} + 230$, when $A_{22}/\nu \sim 5 \times 10^{-9}$, while for the (2,0) mode it occurs at $t \sim t_{A_{22}}^{\text{peak}} + 120$, when $A_{20}/\nu \sim 5 \times 10^{-5}$. For the RWZHyp simulation here considered, we find that the tail is well described by a power-law $h_{20}^{\text{tail}} \propto (t - t_{A_{22}}^{\text{peak}})^{-2.787}$ (see inset of Fig. 3). However, in general, the tail can have rather complicated behaviors, as extensively discussed in Ref. [111]. Eccentric RWZHyp simulations show that the tail enhancement due to the orbital eccentricity observed for the $m > 0$ modes [106, 111, 114, 115] occurs also for the (2,0) mode in Schwarzschild.

By inspecting the SXS catalog [67], we observe an enhancement of the (2,0) oscillatory mode for binaries with anti-aligned spins also in the comparable-mass case. However, as the symmetric mass ratio increases, the null memory contribution gains importance, as it is linked to the radiated energy flux. For the same reason, the memory contribution is enhanced for spin-aligned binaries, where, instead, the oscillatory part is suppressed. The accurate modeling of both contributions is thus needed.

Hilbert post-merger model – IMR models have to be completed with analytical ringdown models built employing NR simulations [18, 19, 68, 116]. In particular, Ref. [68] proposed to factorize the fundamental QNM from the numerical multipoles, thus obtaining a QNM-rescaled mode. The latter is defined as $\bar{h}(\tau) \equiv e^{\sigma_1 \tau + i\phi_0} h(\tau)$, where $\sigma_1 = \alpha_1 + i\omega_1$ is the fundamental QNM, ϕ_0 is the phase at the starting time of the fit t_{fit}^0 , $\tau = (t - t_{\text{fit}}^0)/M_f$, and M_f is the mass of the remnant. This signal thus still contains all the source-driven transient contributions, higher QNM overtones, and eventual non-linearities that are in numerical waveforms. The closed-form description is then achieved by fitting the amplitude and the phase of the rescaled waveform, $\bar{h} = A_{\bar{h}} e^{i\phi_{\bar{h}}}$. The model’s accuracy relies in the simple shape of the amplitude and phase of \bar{h} , which can be easily fitted with activation-like monotonic functions.

While this approach has been successfully adopted for complex modes, it cannot be readily applied to the real $m = 0$ modes due to its inherently complex nature. Moreover, complex signals allows us to impose continuity conditions on amplitude and frequency, which is important for constraining fit parameters and for applying NQC corrections, as we will discuss in the next section. We thus propose to i) complexify the $m = 0$ modes, ii) apply a model similar to the one discussed above, iii) get the physical signal by solely considering the real part.

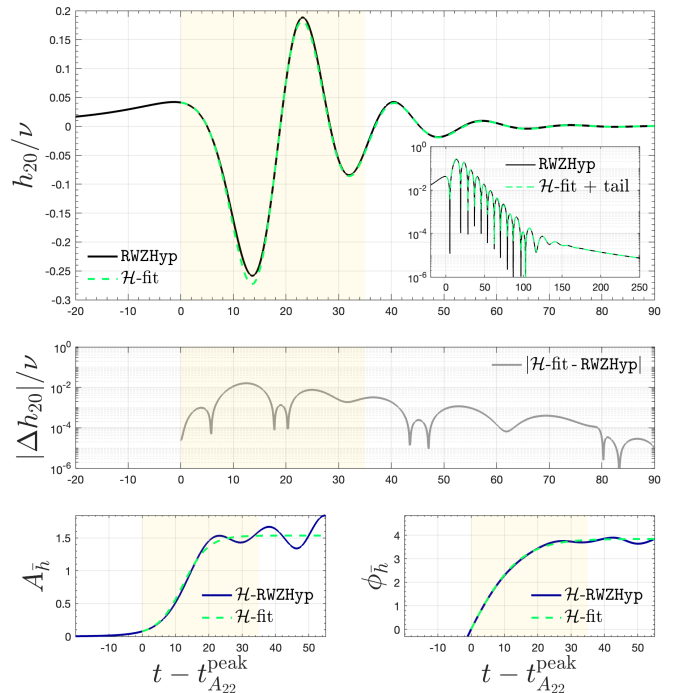


FIG. 3. Upper panel: (2,0) mode for the Schwarzschild configuration. We show the numerical waveform (black) and the Hilbert fit (dashed green). Middle panel: corresponding residual. Bottom panels: QNM-rescaled amplitudes and phase of the complexified numerical (2,0) mode (blue) and corresponding Hilbert fits (dashed green). The vertical bands mark the \mathcal{H} -fitting interval.

To this end, we use the Hilbert transform [69, 70] of a function $v(t)$, defined as $\mathcal{H}[v](t) \equiv 2/\pi \lim_{\epsilon \rightarrow 0} \int_{\epsilon}^{\infty} \frac{v(t-\tau) - v(t+\tau)}{2\tau} d\tau$. Its meaning is clarified by the relation with the Fourier transform $\mathcal{F}[v](\omega)$,

$$\mathcal{F}[\mathcal{H}[v]](\omega) = -i \text{sgn}(\omega) \mathcal{F}[v](\omega), \quad (1)$$

where $\text{sgn}(x)$ is the sign function. Therefore, the Hilbert transform shifts the negative (positive) frequencies of $v(t)$ by $\frac{\pi}{2}$ ($-\frac{\pi}{2}$). Given a real signal $v_{\text{R}}(t)$, the Hilbert transform can be used to create an analytical signal $v_{\mathcal{H}}(t) = v_{\text{R}}(t) - i\mathcal{H}[v](t)$. If we apply this complexification to the $m = 0$ modes, we find amplitudes and phases that *look like* the ones of the $m > 0$ modes. We can thus generalize the phenomenological ringdown model of Ref. [68] to real modes by simply working with their complexifications.

The Hilbert transform has to be performed only when building the model; once the parameters of the ansätze have been found, we can just evaluate the closed-form post-merger waveform.

We start by applying this procedure to the (2,0) mode of the Schwarzschild case. It is known that for complex higher modes that are strongly delayed with respect to the (2,2) one, it is convenient to apply the model of Ref. [68] from $t_{A_{22}}^{\text{peak}}$ rather than from $t_{A_{\ell m}}^{\text{peak}}$ [117]. We thus

¹ Indeed, the tail is enhanced by radial motion; see, e.g., Ref. [111] and Eq. (22) therein or Refs. [112, 113].

perform our Hilbert fit starting from $t_{\text{fit}}^0 = t_{A_{22}}^{\text{peak}}$. This choice facilitates the matching with the inspiral waveform discussed in the next section. The amplitude and phase of the complexified QNM-rescaled waveforms are modeled with ansätze similar to the ones proposed in Ref. [68], as detailed in the SM. Note that some coefficients are constrained in terms of numerical quantities, $\{A_0, \dot{A}_0, \omega_0\}$, by imposing continuity conditions. The results for the Schwarzschild case are displayed in Fig. 3. In the bottom panels we report the amplitude and phase of the complexified numerical waveform (dark blue), together with the primary Hilbert fits (dashed green). The chosen ansätze are able to catch the behavior of the complexified signal, yielding a real (2,0) mode (top panel) with analytical/numerical residual $\lesssim 0.02$ (middle panel). However, it should be noted that the phase template is more accurate than the amplitude one, meaning that future works could explore different choices for the amplitude ansatz to further improve the accuracy of this procedure. Moreover, the oscillations in the complexified signal observed for $t \gtrsim t_{A_{22}}^{\text{peak}} + 20$ are likely to be, at least in part, an artefact of the transform. Indeed, they also appear when complexifying the real part of the (2,2) mode, while they are less evident in the corresponding physical waveform.

The post-merger Hilbert fit can readily be applied to higher modes, Kerr configurations, and NR simulations. While some primary fits performed over SXS simulations are shown in the SM, we build our model for the oscillatory contribution using waveforms generated with NRHybSur3dq8 [54]. Once the coefficients have been found for enough configurations, we can fit them over the parameter space. For the mass and spin of the remnant, we use the fits of Refs. [118, 119], while for the coefficients of the new model and $\{A_0, \dot{A}_0, \omega_0\}$ we perform a hierarchical fit. We first perform quadratic fits of test-mass and non-spinning configurations, separately. We then complete our model by merging these two results over the parameter space identified by (ν, \tilde{a}_0) , where $\tilde{a}_0 = (m_1 \chi_1 + m_2 \chi_2)/M$ generalizes the Kerr spin. The explicit ansätze and the coefficients found are given in the SM.

Matching with inspiral waveform – A formally Newtonian expression for the inspiral $m = 0$ modes can be obtained following Ref. [26]. For the (2,0) mode, this reads

$$h_{20}^{\text{inspl}} = 4 \sqrt{\frac{2\pi}{15}} \nu (r\ddot{r} + \dot{r}^2). \quad (2)$$

Note that 2.5PN corrections for h_{20}^{inspl} have been recently computed [81, 120] and might be useful for generic orbits. However, since here we are focusing on the plunge of quasi-circular evolutions, we do not consider them².

To match this waveform to the post-merger model previously discussed, we can also complexify h_{20}^{inspl} with a Hilbert transform. The matching can be then performed with standard EOB techniques, which involve NQC corrections. Note that for NQC corrections to work effectively, well-defined and preferably monotonic amplitude and phase are needed. We achieve these requirements through the aforementioned complexification. Although this matching is a standard procedure in EOB models, we briefly discuss it in the SM for completeness, along with minor technical details.

Null memory effects – Null memory effects [71–74], which are particularly relevant for comparable mass binaries, can be computed using BMS balance laws [92]. These relations connect the strain to the Bondi aspects (*i.e.*, the oscillatory parts discussed so far) and the radiated fluxes. More specifically, the displacement memory in the (2,0) mode arises from the supertranslation conservation law, and is thus sourced by the radiated energy flux. It can be written in terms of the most relevant multipoles as [94]

$$\begin{aligned} h_{20}^{\text{memo}}(t) = & \frac{1}{7} \sqrt{\frac{5}{6\pi}} \int_{t_0}^t |\dot{h}_{22}|^2 dt - \frac{1}{14} \sqrt{\frac{5}{6\pi}} \int_{t_0}^t |\dot{h}_{21}|^2 dt \\ & + \frac{5}{2\sqrt{42\pi}} \int_{t_0}^t (\dot{h}_{22}^{\text{Re}} \dot{h}_{32}^{\text{Re}} + \dot{h}_{22}^{\text{Im}} \dot{h}_{32}^{\text{Im}}) \\ & - \frac{2}{11} \sqrt{\frac{2}{15\pi}} \int_{t_0}^t |\dot{h}_{44}|^2 dt. \end{aligned} \quad (3)$$

Formally, one should consider $t_0 \rightarrow -\infty$, but in practical application t_0 is the starting time of the evolution. This means that, if we extrapolate back in time, we get the unphysical property $h_{20}^{\text{memo}} \neq 0$ for $t \rightarrow -\infty$. This can easily be fixed by matching this memory contribution to the PN formula [75, 76], which correctly vanishes at zero frequency. Note that Ref. [94] followed a similar approach. Technical details on this matching are discussed in the SM. Therefore, given the $m > 0$ EOB multipoles, we can compute the full (2,0) mode as $h_{20} = h_{20}^{\text{osc}} + h_{20}^{\text{memo}}$, where h_{20}^{osc} is the oscillatory contribution previously discussed.

EOB/NR comparisons – We now apply the methodology here introduced to the EOB model **TEOBResumS-GIOTTO** [14] and compare it with NR results. To avoid ambiguities linked to different BMS frames, we consider the surrogate NRHybSur3dq8_CCE [13], whose waveforms are already in the PN frame, as the EOB ones. Time-domain comparisons for two meaningful equal mass cases are reported in Fig. 4, showing that our model is able to capture the main features of the numerical waveform. Since the ringdown modeling of the higher modes enter in the computation of the final EOB offset, improving their description would yield an offset closer to the numerical one. This is however beyond the scope of this work, and thus deferred to future investigations. Some additional time-domain comparisons are reported in the SM. To assess the accuracy more systematically,

² Moreover, PN results are known to be unreliable in the late stages of the evolution.

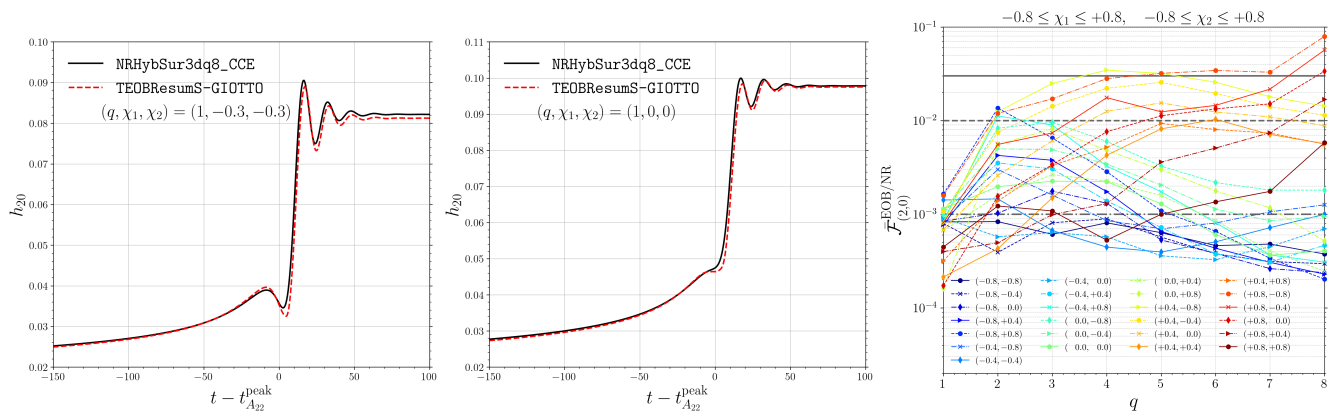


FIG. 4. Comparisons of $(2,0)$ modes given by NRHybSur3dq8_CCE and the ones computed in this work using TEOBResumS-GIOTTO as a baseline. Left and middle panels: time-domain comparisons. Right panel: LIGO-weighted mismatches of the $(2,0)$ modes for different mass ratios and spin configurations. The legend in the right panel reports (χ_1, χ_2) .

we also consider frequency-domain mismatches for the $(2,0)$ mode for different mass-ratios and spins in the right panel of Fig. 4. We consider the noise curve of Advance LIGO [121] and a reference mass of $50M_\odot$. More technical details are reported in the SM. The model is generally accurate, especially for equal-mass binaries, where all the mismatches are below 2×10^{-3} , and for high mass-ratio cases with low spins. However, higher mismatches are obtained for configurations where χ_1 and χ_2 strongly differ. This can be understood by considering that we reduce the dimensionality of the fits across the parameter space by employing the effective spin \tilde{a}_0 rather than the two individual spins $\chi_{1,2}$ separately.

We conclude by discussing the quadrupolar strains anticipated in Fig. 1, which are computed for an observer with line of sight that maximizes the contribution of the $(2,0)$ mode ($\Theta = \frac{\pi}{2}$). We compare our EOB model with the results from NRHybSur3dq8_CCE and the equal mass nonspinning simulation of the ExtCCE SXS catalog [12]. Note that the SXS waveform is not in the PN frame, but we can obtain a good agreement with the surrogate by i) mapping it to the superrest frame with the package scri [122–125], ii) shifting its $(2,0)$ mode in order to match the final offset of the surrogate model. A more accurate, though more complex, procedure would involve mapping the SXS waveform to the PN frame as detailed in Refs. [12, 102]. We remark that no additional offset-shifting is performed for the EOB and NRHybSur3dq8_CCE waveforms. The agreement between the three shows the goodness of TEOBResumS-GIOTTO completed with the $(2,0)$ mode as discussed in this work. The EOB/NR mismatch for the complete quadrupolar waveform in this case is $\bar{\mathcal{F}} = 6 \times 10^{-4}$.

Conclusions – We have proposed a method to include the description of the real $m = 0$ modes in the EOB framework, thus completing the multipolar structure of IMR EOB waveforms for spin-aligned quasi-circular BBHs. In particular, we have discussed how to model the oscillatory post-merger of such modes by first

complexifying them with a Hilbert transform, and then using a post-merger ansatz based on Ref. [68], as typically done for $m > 0$ modes. We thus effectively include source-driven and higher QNM overtones contributions. This model has been applied to a set of test-mass simulations, hence showing its applicability in the linear perturbation regime. We then focused on the $(2,0)$ modes and discussed how to employ NQC corrections to match the Hilbert post-merger model to the inspiral EOB waveform obtained with the approach introduced in Ref. [26]. The close-form description of the $(2,0)$ post-merger for the comparable mass case has been achieved by performing hierarchical fits for different mass ratios and effective spins using waveforms from NRHybSur3dq8 [54]. These fits correctly include the test-mass limit. We have then discussed how to include null memory effects in EOB models, thus providing a complete description of the $(2,0)$ mode. Following this prescription, we have complemented TEOBResumS-GIOTTO and tested its validity against the surrogate NRHybSur3dq8_CCE [13]. We also performed a comparison with the equal mass nonspinning configuration of the SXS catalog of Ref. [12], showing a remarkable agreement.

Future works will focus on refining the methodology here introduced and on employing it to complete EOB models where the relevance of the $(2,0)$ mode is even more enhanced than for spin-aligned quasi-circular binaries, such as precessing and eccentric models [44].

Acknowledgment – S.A. is grateful to R. Gamba, S. Bernuzzi and A. Nagar for useful discussions through the whole development of this work. S.A. also thanks G. Carullo and M. De Amicis for useful comments and suggestions on the draft. S.A. acknowledges support from the Deutsche Forschungsgemeinschaft (DFG) project “GROOVHY” (BE 6301/5-1 Projektnummer: 523180871). The EOB model TEOBResumS-GIOTTO and its version for generic orbital motion, TEOBResumS-Dalí, are publicly available at <https://bitbucket.org/teobresums/teobresums/src/>. However, the procedure for computing

the (2,0) mode described in this work has not yet been

implemented in the public code. In Fig. 2, we used a scientific colormap provided by Ref. [126].

-
- [1] J. Aasi *et al.* (LIGO Scientific), *Class. Quant. Grav.* **32**, 074001 (2015), [arXiv:1411.4547 \[gr-qc\]](#).
 - [2] F. Acernese *et al.* (VIRGO), *Class. Quant. Grav.* **32**, 024001 (2015), [arXiv:1408.3978 \[gr-qc\]](#).
 - [3] B. P. Abbott *et al.* (LIGO Scientific, Virgo), *Phys. Rev. X* **9**, 031040 (2019), [arXiv:1811.12907 \[astro-ph.HE\]](#).
 - [4] R. Abbott *et al.* (LIGO Scientific, Virgo), *Phys. Rev. X* **11**, 021053 (2021), [arXiv:2010.14527 \[gr-qc\]](#).
 - [5] R. Abbott *et al.* (LIGO Scientific, VIRGO, KAGRA), (2021), [arXiv:2111.03606 \[gr-qc\]](#).
 - [6] M. Punturo, M. Abernathy, F. Acernese, B. Allen, N. Andersson, *et al.*, *Class. Quant. Grav.* **27**, 194002 (2010).
 - [7] M. Maggiore *et al.*, *JCAP* **03**, 050 (2020), [arXiv:1912.02622 \[astro-ph.CO\]](#).
 - [8] P. Amaro-Seoane *et al.* (LISA), (2017), [arXiv:1702.00786 \[astro-ph.IM\]](#).
 - [9] D. Reitze *et al.*, *Bull. Am. Astron. Soc.* **51**, 035 (2019), [arXiv:1907.04833 \[astro-ph.IM\]](#).
 - [10] M. Pürrer and C.-J. Haster, *Phys. Rev. Res.* **2**, 023151 (2020), [arXiv:1912.10055 \[gr-qc\]](#).
 - [11] A. Gupta *et al.*, (2024), [arXiv:2405.02197 \[gr-qc\]](#).
 - [12] K. Mitman *et al.*, *Phys. Rev. D* **104**, 024051 (2021), [arXiv:2105.02300 \[gr-qc\]](#).
 - [13] J. Yoo *et al.*, *Phys. Rev. D* **108**, 064027 (2023), [arXiv:2306.03148 \[gr-qc\]](#).
 - [14] A. Nagar, P. Retteno, R. Gamba, S. Albanesi, A. Albertini, and S. Bernuzzi, *Phys. Rev. D* **108**, 124018 (2023), [arXiv:2304.09662 \[gr-qc\]](#).
 - [15] A. Buonanno and T. Damour, *Phys. Rev.* **D59**, 084006 (1999), [arXiv:gr-qc/9811091](#).
 - [16] A. Buonanno and T. Damour, *Phys. Rev.* **D62**, 064015 (2000), [arXiv:gr-qc/0001013](#).
 - [17] T. Damour, *Phys. Rev.* **D64**, 124013 (2001), [arXiv:gr-qc/0103018](#).
 - [18] A. Buonanno, G. B. Cook, and F. Pretorius, *Phys. Rev. D* **75**, 124018 (2007), [arXiv:gr-qc/0610122](#).
 - [19] T. Damour and A. Nagar, *Phys. Rev.* **D76**, 064028 (2007), [arXiv:0705.2519 \[gr-qc\]](#).
 - [20] T. Damour, A. Nagar, E. N. Dorband, D. Pollney, and L. Rezzolla, *Phys. Rev.* **D77**, 084017 (2008), [arXiv:0712.3003 \[gr-qc\]](#).
 - [21] L. Pompili *et al.*, *Phys. Rev. D* **108**, 124035 (2023), [arXiv:2303.18039 \[gr-qc\]](#).
 - [22] T. Damour and A. Nagar, *Phys. Rev.* **D81**, 084016 (2010), [arXiv:0911.5041 \[gr-qc\]](#).
 - [23] T. Damour, A. Nagar, and L. Villain, *Phys. Rev.* **D85**, 123007 (2012), [arXiv:1203.4352 \[gr-qc\]](#).
 - [24] A. Nagar *et al.*, *Phys. Rev.* **D98**, 104052 (2018), [arXiv:1806.01772 \[gr-qc\]](#).
 - [25] T. Dietrich *et al.*, *Phys. Rev.* **D99**, 024029 (2019), [arXiv:1804.02235 \[gr-qc\]](#).
 - [26] D. Chiamello and A. Nagar, *Phys. Rev. D* **101**, 101501 (2020), [arXiv:2001.11736 \[gr-qc\]](#).
 - [27] A. Nagar, P. Retteno, R. Gamba, and S. Bernuzzi, *Phys. Rev. D* **103**, 064013 (2021), [arXiv:2009.12857 \[gr-qc\]](#).
 - [28] A. Nagar, A. Bonino, and P. Retteno, *Phys. Rev. D* **103**, 104021 (2021), [arXiv:2101.08624 \[gr-qc\]](#).
 - [29] M. Khalil, A. Buonanno, J. Steinhoff, and J. Vines, *Phys. Rev. D* **104**, 024046 (2021), [arXiv:2104.11705 \[gr-qc\]](#).
 - [30] A. Placidi, S. Albanesi, A. Nagar, M. Orselli, S. Bernuzzi, and G. Grignani, *Phys. Rev. D* **105**, 104030 (2022), [arXiv:2112.05448 \[gr-qc\]](#).
 - [31] A. Ramos-Buades, A. Buonanno, M. Khalil, and S. Ossokine, *Phys. Rev. D* **105**, 044035 (2022), [arXiv:2112.06952 \[gr-qc\]](#).
 - [32] S. Albanesi, A. Placidi, A. Nagar, M. Orselli, and S. Bernuzzi, *Phys. Rev. D* **105**, L121503 (2022), [arXiv:2203.16286 \[gr-qc\]](#).
 - [33] A. Nagar, R. Gamba, P. Retteno, V. Fantini, and S. Bernuzzi, *Phys. Rev. D* **110**, 084001 (2024), [arXiv:2404.05288 \[gr-qc\]](#).
 - [34] A. Nagar, D. Chiamello, R. Gamba, S. Albanesi, S. Bernuzzi, V. Fantini, M. Panzeri, and P. Retteno, *Phys. Rev. D* **111**, 064050 (2025), [arXiv:2407.04762 \[gr-qc\]](#).
 - [35] A. Buonanno, Y. Chen, and T. Damour, *Phys. Rev.* **D74**, 104005 (2006), [arXiv:gr-qc/0508067](#).
 - [36] Y. Pan, A. Buonanno, A. Taracchini, L. E. Kidder, A. H. Mroue, *et al.*, *Phys. Rev.* **D89**, 084006 (2014), [arXiv:1307.6232 \[gr-qc\]](#).
 - [37] S. Akcay, R. Gamba, and S. Bernuzzi, *Phys. Rev. D* **103**, 024014 (2021), [arXiv:2005.05338 \[gr-qc\]](#).
 - [38] R. Gamba, S. Akcay, S. Bernuzzi, and J. Williams, *Phys. Rev. D* **106**, 024020 (2022), [arXiv:2111.03675 \[gr-qc\]](#).
 - [39] M. Khalil, A. Buonanno, H. Estelles, D. P. Mihaylov, S. Ossokine, L. Pompili, and A. Ramos-Buades, *Phys. Rev. D* **108**, 124036 (2023), [arXiv:2303.18143 \[gr-qc\]](#).
 - [40] A. Ramos-Buades, A. Buonanno, H. Estellés, M. Khalil, D. P. Mihaylov, S. Ossokine, L. Pompili, and M. Shiferaw, *Phys. Rev. D* **108**, 124037 (2023), [arXiv:2303.18046 \[gr-qc\]](#).
 - [41] A. Gonzalez, R. Gamba, M. Breschi, F. Zappa, G. Carullo, S. Bernuzzi, and A. Nagar, *Phys. Rev. D* **107**, 084026 (2023), [arXiv:2212.03909 \[gr-qc\]](#).
 - [42] R. Gamba and S. Bernuzzi, *Phys. Rev. D* **107**, 044014 (2023), [arXiv:2207.13106 \[gr-qc\]](#).
 - [43] R. Gamba *et al.*, (2023), [arXiv:2307.15125 \[gr-qc\]](#).
 - [44] R. Gamba, D. Chiamello, and S. Neogi, *Phys. Rev. D* **110**, 024031 (2024), [arXiv:2404.15408 \[gr-qc\]](#).
 - [45] T. Regge and J. A. Wheeler, *Phys. Rev.* **108**, 1063 (1957).
 - [46] F. J. Zerilli, *Phys. Rev. Lett.* **24**, 737 (1970).
 - [47] A. Nagar and L. Rezzolla, *Class. Quant. Grav.* **22**, R167 (2005), [arXiv:gr-qc/0502064](#).
 - [48] K. Martel and E. Poisson, *Physical Review D (Particles, Fields, Gravitation, and Cosmology)* **71**, 104003 (2005).
 - [49] S. A. Teukolsky, *Astrophys. J.* **185**, 635 (1973).
 - [50] S. Bernuzzi and A. Nagar, *Phys. Rev.* **D81**, 084056 (2010), [arXiv:1003.0597 \[gr-qc\]](#).
 - [51] S. Bernuzzi, A. Nagar, and A. Zenginoglu, *Phys. Rev.*

- D84**, 084026 (2011), [arXiv:1107.5402 \[gr-qc\]](#).
- [52] S. Bernuzzi, A. Nagar, and A. Zenginoglu, *Phys. Rev. D* **86**, 104038 (2012), [arXiv:1207.0769 \[gr-qc\]](#).
- [53] E. Harms, S. Bernuzzi, A. Nagar, and A. Zenginoglu, *Class. Quant. Grav.* **31**, 245004 (2014), [arXiv:1406.5983 \[gr-qc\]](#).
- [54] V. Varma, S. E. Field, M. A. Scheel, J. Blackman, L. E. Kidder, and H. P. Pfeiffer, *Phys. Rev. D* **99**, 064045 (2019), [arXiv:1812.07865 \[gr-qc\]](#).
- [55] T. Chu, H. P. Pfeiffer, and M. A. Scheel, *Phys. Rev. D* **80**, 124051 (2009), [arXiv:0909.1313 \[gr-qc\]](#).
- [56] G. Lovelace, M. Scheel, and B. Szilagyi, *Phys. Rev. D* **83**, 024010 (2011), [arXiv:1010.2777 \[gr-qc\]](#).
- [57] G. Lovelace, M. Boyle, M. A. Scheel, and B. Szilagyi, *Class. Quant. Grav.* **29**, 045003 (2012), [arXiv:1110.2229 \[gr-qc\]](#).
- [58] L. T. Buchman, H. P. Pfeiffer, M. A. Scheel, and B. Szilagyi, *Phys. Rev. D* **86**, 084033 (2012), [arXiv:1206.3015 \[gr-qc\]](#).
- [59] D. A. Hemberger, G. Lovelace, T. J. Loredo, L. E. Kidder, M. A. Scheel, B. Szilagyi, N. W. Taylor, and S. A. Teukolsky, *Phys. Rev. D* **88**, 064014 (2013), [arXiv:1305.5991 \[gr-qc\]](#).
- [60] M. A. Scheel, M. Giesler, D. A. Hemberger, G. Lovelace, K. Kuper, M. Boyle, B. Szilagyi, and L. E. Kidder, *Class. Quant. Grav.* **32**, 105009 (2015), [arXiv:1412.1803 \[gr-qc\]](#).
- [61] J. Blackman, S. E. Field, C. R. Galley, B. Szilagyi, M. A. Scheel, M. Tiglio, and D. A. Hemberger, *Phys. Rev. Lett.* **115**, 121102 (2015), [arXiv:1502.07758 \[gr-qc\]](#).
- [62] G. Lovelace *et al.*, *Class. Quant. Grav.* **32**, 065007 (2015), [arXiv:1411.7297 \[gr-qc\]](#).
- [63] A. H. Mroue, M. A. Scheel, B. Szilagyi, H. P. Pfeiffer, M. Boyle, *et al.*, *Phys. Rev. Lett.* **111**, 241104 (2013), [arXiv:1304.6077 \[gr-qc\]](#).
- [64] P. Kumar, K. Barkett, S. Bhagwat, N. Afshari, D. A. Brown, G. Lovelace, M. A. Scheel, and B. Szilagyi, *Phys. Rev. D* **92**, 102001 (2015), [arXiv:1507.00103 \[gr-qc\]](#).
- [65] T. Chu, H. Fong, P. Kumar, H. P. Pfeiffer, M. Boyle, D. A. Hemberger, L. E. Kidder, M. A. Scheel, and B. Szilagyi, *Class. Quant. Grav.* **33**, 165001 (2016), [arXiv:1512.06800 \[gr-qc\]](#).
- [66] M. Boyle *et al.*, *Class. Quant. Grav.* **36**, 195006 (2019), [arXiv:1904.04831 \[gr-qc\]](#).
- [67] “SXS Gravitational Waveform Database,” <https://data.black-holes.org/waveforms/index.html>.
- [68] T. Damour and A. Nagar, *Phys. Rev. D* **90**, 024054 (2014), [arXiv:1406.0401 \[gr-qc\]](#).
- [69] D. Hilbert, *Grundzüge einer allgemeinen Theorie der linearen Integralgleichungen* (B.G. Teubner, Leipzig, 1912).
- [70] R. N. Bracewell, *The Fourier Transform and Its Applications* (McGraw-Hill, 2000).
- [71] D. Christodoulou, *Phys. Rev. Lett.* **67**, 1486 (1991).
- [72] K. S. Thorne, *Phys. Rev. D* **45**, 520 (1992).
- [73] L. Blanchet and T. Damour, *Phys. Rev. D* **46**, 4304 (1992).
- [74] K. Mitman *et al.*, *Class. Quant. Grav.* **41**, 223001 (2024), [arXiv:2405.08868 \[gr-qc\]](#).
- [75] M. Favata, *Phys. Rev. D* **80**, 024002 (2009), [arXiv:0812.0069 \[gr-qc\]](#).
- [76] K. Cunningham, C. Kavanagh, A. Pound, D. Trestini, N. Warburton, and J. Neef, (2024), [arXiv:2410.23950 \[gr-qc\]](#).
- [77] M. Favata, *Astrophys. J. Lett.* **696**, L159 (2009), [arXiv:0902.3660 \[astro-ph.SR\]](#).
- [78] M. Favata, *Class. Quant. Grav.* **27**, 084036 (2010), [arXiv:1003.3486 \[gr-qc\]](#).
- [79] M. Favata, *Phys. Rev. D* **84**, 124013 (2011), [arXiv:1108.3121 \[gr-qc\]](#).
- [80] M. Ebersold, Y. Boetzel, G. Faye, C. K. Mishra, B. R. Iyer, and P. Jetzer, *Phys. Rev. D* **100**, 084043 (2019), [arXiv:1906.06263 \[gr-qc\]](#).
- [81] E. Grilli, A. Placidi, S. Albanesi, G. Grignani, and M. Orselli, *Phys. Rev. D* **111**, 044045 (2025), [arXiv:2410.05386 \[gr-qc\]](#).
- [82] D. Pollney and C. Reisswig, *Astrophys. J. Lett.* **732**, L13 (2011), [arXiv:1004.4209 \[gr-qc\]](#).
- [83] K. Mitman, J. Moxon, M. A. Scheel, S. A. Teukolsky, M. Boyle, N. Deppe, L. E. Kidder, and W. Throwe, *Phys. Rev. D* **102**, 104007 (2020), [arXiv:2007.11562 \[gr-qc\]](#).
- [84] N. T. Bishop, R. Gomez, L. Lehner, and J. Winicour, *Phys. Rev. D* **54**, 6153 (1996).
- [85] C. Reisswig, N. T. Bishop, D. Pollney, and B. Szilagyi, *Class. Quant. Grav.* **27**, 075014 (2010), [arXiv:0912.1285 \[gr-qc\]](#).
- [86] J. Moxon, M. A. Scheel, and S. A. Teukolsky, *Phys. Rev. D* **102**, 044052 (2020), [arXiv:2007.01339 \[gr-qc\]](#).
- [87] J. Moxon, M. A. Scheel, S. A. Teukolsky, N. Deppe, N. Fischer, F. Hébert, L. E. Kidder, and W. Throwe, *Phys. Rev. D* **107**, 064013 (2023), [arXiv:2110.08635 \[gr-qc\]](#).
- [88] N. Deppe, W. Throwe, L. E. Kidder, N. L. Vu, K. C. Nelli, C. Armaza, M. S. Bonilla, F. Hébert, Y. Kim, P. Kumar, G. Lovelace, A. Macedo, J. Moxon, E. O’Shea, H. P. Pfeiffer, M. A. Scheel, S. A. Teukolsky, N. A. Wittek, I. Anantpurkar, C. Anderson, M. Boyle, A. Carpenter, A. Ceja, H. Chaudhary, N. Corso, F. Foucart, N. Ghadiri, M. Giesler, J. S. Guo, D. A. B. Iozzo, K. Z. Jones, G. Lara, I. Legred, D. Li, S. Ma, D. Melchor, M. Morales, E. R. Most, P. J. Nee, A. Osorio, M. A. Pajkos, K. Pannone, T. Ramirez, N. Ring, H. R. Rüter, J. Sanchez, L. C. Stein, D. Tellez, S. Thomas, D. Vieira, T. Wlodarczyk, D. Wu, and J. Yoo, “Spectre,” (2024).
- [89] H. Bondi, M. G. J. van der Burg, and A. W. K. Metzner, *Proceedings of the Royal Society of London Series A* **269**, 21 (1962).
- [90] R. K. Sachs, *Proceedings of the Royal Society of London Series A* **270**, 103 (1962).
- [91] C. Talbot, E. Thrane, P. D. Lasky, and F. Lin, *Phys. Rev. D* **98**, 064031 (2018), [arXiv:1807.00990 \[astro-ph.HE\]](#).
- [92] K. Mitman *et al.*, *Phys. Rev. D* **103**, 024031 (2021), [arXiv:2011.01309 \[gr-qc\]](#).
- [93] Z. Cao and W.-B. Han, *Class. Quant. Grav.* **33**, 155011 (2016).
- [94] M. Rosselló-Sastre, S. Husa, and S. Bera, *Phys. Rev. D* **110**, 084074 (2024), [arXiv:2405.17302 \[gr-qc\]](#).
- [95] O. M. Boersma, D. A. Nichols, and P. Schmidt, *Phys. Rev. D* **101**, 083026 (2020), [arXiv:2002.01821 \[astro-ph.HE\]](#).
- [96] M. Hübner, C. Talbot, P. D. Lasky, and E. Thrane, *Phys. Rev. D* **101**, 023011 (2020), [arXiv:1911.12496 \[astro-ph.HE\]](#).
- [97] A. M. Grant and D. A. Nichols, *Phys. Rev. D* **107**,

- 064056 (2023), [Erratum: Phys.Rev.D 108, 029901 (2023)], [arXiv:2210.16266 \[gr-qc\]](#).
- [98] B. Goncharov, L. Donnay, and J. Harms, *Phys. Rev. Lett.* **132**, 241401 (2024), [arXiv:2310.10718 \[gr-qc\]](#).
- [99] S. Gasparotto, R. Vicente, D. Blas, A. C. Jenkins, and E. Barausse, *Phys. Rev. D* **107**, 124033 (2023), [arXiv:2301.13228 \[gr-qc\]](#).
- [100] H. Inchauspé, S. Gasparotto, D. Blas, L. Heisenberg, J. Zosso, and S. Tiwari, *Phys. Rev. D* **111**, 044044 (2025), [arXiv:2406.09228 \[gr-qc\]](#).
- [101] Y. Xu, M. Rosselló-Sastre, S. Tiwari, M. Ebersold, E. Z. Hamilton, C. García-Quirós, H. Estellés, and S. Husa, *Phys. Rev. D* **109**, 123034 (2024), [arXiv:2403.00441 \[gr-qc\]](#).
- [102] K. Mitman *et al.*, *Phys. Rev. D* **106**, 084029 (2022), [arXiv:2208.04356 \[gr-qc\]](#).
- [103] A. Pound, *Fund. Theor. Phys.* **179**, 399 (2015), [arXiv:1506.06245 \[gr-qc\]](#).
- [104] S. Bernuzzi, A. Nagar, and A. Zenginoglu, *Phys. Rev. D* **83**, 064010 (2011), [arXiv:1012.2456 \[gr-qc\]](#).
- [105] A. Taracchini, A. Buonanno, G. Khanna, and S. A. Hughes, *Phys. Rev. D* **90**, 084025 (2014), [arXiv:1404.1819 \[gr-qc\]](#).
- [106] S. Albanesi, S. Bernuzzi, T. Damour, A. Nagar, and A. Placidi, *Phys. Rev. D* **108**, 084037 (2023), [arXiv:2305.19336 \[gr-qc\]](#).
- [107] A. Ori and K. S. Thorne, *Phys. Rev. D* **62**, 124022 (2000), [arXiv:gr-qc/0003032 \[gr-qc\]](#).
- [108] R. H. Price, *Phys. Rev. D* **5**, 2419 (1972).
- [109] E. W. Leaver, *Phys. Rev. D* **34**, 384 (1986).
- [110] N. Andersson, *Phys. Rev. D* **55**, 468 (1997), [arXiv:gr-qc/9607064](#).
- [111] M. De Amicis, S. Albanesi, and G. Carullo, *Phys. Rev. D* **110**, 104005 (2024), [arXiv:2406.17018 \[gr-qc\]](#).
- [112] M. De Amicis *et al.*, (2024), [arXiv:2412.06887 \[gr-qc\]](#).
- [113] S. Ma, M. A. Scheel, J. Moxon, K. C. Nelli, N. Deppe, L. E. Kidder, W. Throwe, and N. L. Vu, (2024), [arXiv:2412.06906 \[gr-qc\]](#).
- [114] V. Cardoso, G. Carullo, M. De Amicis, F. Duque, T. Katagiri, D. Pereniguez, J. Redondo-Yuste, T. F. M. Spieksma, and Z. Zhong, *Phys. Rev. D* **109**, L121502 (2024), [arXiv:2405.12290 \[gr-qc\]](#).
- [115] T. Islam, G. Faggioli, G. Khanna, S. E. Field, M. van de Meent, and A. Buonanno, (2024), [arXiv:2407.04682 \[gr-qc\]](#).
- [116] J. G. Baker *et al.*, *Phys. Rev. D* **78**, 044046 (2008), [arXiv:0805.1428 \[gr-qc\]](#).
- [117] R. Cotesta, A. Buonanno, A. Bohé, A. Taracchini, I. Hinder, and S. Ossokine, *Phys. Rev. D* **98**, 084028 (2018), [arXiv:1803.10701 \[gr-qc\]](#).
- [118] X. Jiménez-Forteza, D. Keitel, S. Husa, M. Hannam, S. Khan, and M. Pürrer, *Phys. Rev. D* **95**, 064024 (2017), [arXiv:1611.00332 \[gr-qc\]](#).
- [119] A. Nagar, G. Riemenschneider, G. Pratten, P. Retegno, and F. Messina, *Phys. Rev. D* **102**, 024077 (2020), [arXiv:2001.09082 \[gr-qc\]](#).
- [120] A. Placidi, G. Grignani, T. Harmark, M. Orselli, S. Glorio, and A. Nagar, *Phys. Rev. D* **108**, 024068 (2023), [arXiv:2305.14440 \[gr-qc\]](#).
- [121] “Updated Advanced LIGO sensitivity design curve,” <https://dcc.ligo.org/LIGO-T1800044/public>.
- [122] M. Boyle, *Phys. Rev. D* **87**, 104006 (2013), [arXiv:1302.2919 \[gr-qc\]](#).
- [123] M. Boyle, L. E. Kidder, S. Ossokine, and H. P. Pfeiffer, (2014), [arXiv:1409.4431 \[gr-qc\]](#).
- [124] M. Boyle, *Phys. Rev. D* **93**, 084031 (2016), [arXiv:1509.00862 \[gr-qc\]](#).
- [125] M. Boyle, D. Iozzo, and L. C. Stein, “moble/scri: v1.2,” (2020).
- [126] F. Cramer, “Scientific colour maps,” (2023).
- [127] C. J. Woodford, M. Boyle, and H. P. Pfeiffer, *Phys. Rev. D* **100**, 124010 (2019), [arXiv:1904.04842 \[gr-qc\]](#).
- [128] J. Healy, C. O. Lousto, Y. Zlochower, and M. Campanelli, *Class. Quant. Grav.* **34**, 224001 (2017), [arXiv:1703.03423 \[gr-qc\]](#).
- [129] J. Healy, C. O. Lousto, J. Lange, R. O’Shaughnessy, Y. Zlochower, and M. Campanelli, *Phys. Rev. D* **100**, 024021 (2019), [arXiv:1901.02553 \[gr-qc\]](#).
- [130] J. Healy and C. O. Lousto, *Phys. Rev. D* **102**, 104018 (2020), [arXiv:2007.07910 \[gr-qc\]](#).
- [131] J. Healy and C. O. Lousto, *Phys. Rev. D* **105**, 124010 (2022), [arXiv:2202.00018 \[gr-qc\]](#).
- [132] S. Albanesi, A. Nagar, and S. Bernuzzi, *Phys. Rev. D* **104**, 024067 (2021), [arXiv:2104.10559 \[gr-qc\]](#).
- [133] T. Damour, B. R. Iyer, and A. Nagar, *Phys. Rev. D* **79**, 064004 (2009), [arXiv:0811.2069 \[gr-qc\]](#).
- [134] T. Damour and A. Nagar, *Phys. Rev. D* **90**, 044018 (2014), [arXiv:1406.6913 \[gr-qc\]](#).
- [135] C. Bower, C. D. Capano, S. De, M. Cabero, D. A. Brown, A. H. Nitz, and V. Raymond, *Publ. Astron. Soc. Pac.* **131**, 024503 (2019), [arXiv:1807.10312 \[astro-ph.IM\]](#).
- [136] Y. Chen *et al.*, *Phys. Rev. D* **110**, 064049 (2024), [arXiv:2405.06197 \[gr-qc\]](#).
- [137] J. Valencia, R. Tenorio, M. Rosselló-Sastre, and S. Husa, *Phys. Rev. D* **110**, 124026 (2024), [arXiv:2406.16636 \[gr-qc\]](#).
- [138] I. Harry, J. Calderón Bustillo, and A. Nitz, *Phys. Rev. D* **97**, 023004 (2018), [arXiv:1709.09181 \[gr-qc\]](#).

SUPPLEMENTAL MATERIAL

Primary ansätze for the Hilbert fit – We report here the explicit expressions used for the primary fits of the amplitude and phase of the QNM-rescaled waveform [68, 117]. They read

$$A_{\bar{h}} = c_1^A \tanh(c_2^A \tau + c_3^A) + c_4^A, \quad (4)$$

$$\phi_{\bar{h}} = -c_1^\phi \ln \left(\frac{1 + c_3^\phi e^{-c_2^\phi \tau}}{1 + c_3^\phi} \right), \quad (5)$$

where $\tau = (t - t_{\text{fit}}^0)/M_f$, and M_f is the mass of the remnant. By imposing continuity conditions at t_{fit}^0 , we constrain the following parameters:

$$c_1^A = \left(\dot{A}_0 + \alpha_1 A_0 \right) \frac{1}{c_2^A} \cosh(c_3^A)^2, \quad (6)$$

$$c_4^A = A_0 - \left(\dot{A}_0 + \alpha_1 A_0 \right) \frac{1}{c_2^A} \cosh(c_3^A) \sinh(c_3^A), \quad (7)$$

$$c_1^\phi = \frac{1 + c_3^\phi}{c_2^\phi c_3^\phi} (\omega_1 - M_f \omega_0), \quad (8)$$

where we recall that the fundamental QNM frequency is denoted as $\sigma_1 = \alpha_1 + i\omega_1$, while ω_0 is the waveform

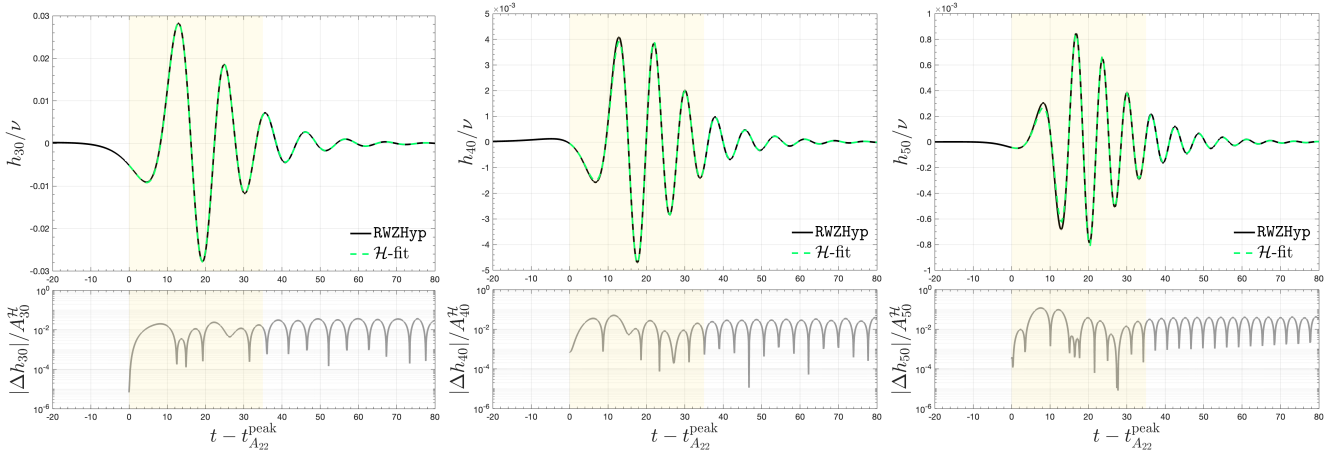


FIG. 5. RWZHyP (3,0), (4,0) and (5,0) waveforms generated by the inspiral-plunge-merger of a test particle in Schwarzschild (black), together with the corresponding Hilbert fits (dashed green). In the bottom panels we report the analytical/numerical residuals normalized with the amplitude of the complexified signals. The vertical bands mark the \mathcal{H} -fitting interval.

frequency at $t = t_{\text{fit}}^0$. The (2,0) multipole has been already discussed in the main text. In Fig. 5 we report, instead, the results for the (3,0), (4,0), and (5,0) modes in the Schwarzschild case. We also show the residuals in the bottom panels, but since the amplitude of the modes varies of different order of magnitudes, we normalize them with the amplitude of the complexified signal. As can be seen, the accuracy of the Hilbert fit remains consistent also for the higher modes. For Kerr, we consider primary fits of the (2,0) mode up to $\hat{a} = 0.6$. The coefficients found are reported in Table II.

We now turn our attention to the comparable mass case. We report some significant cases of Hilbert fits performed over SXS data of the public catalog [67] in Fig. 6. The numerical waveforms are extracted at finite distance and then extrapolated, so that null memory effects are not captured. In other words, these numerical data only represent the Bondi mass aspect and, as a consequence, can be fitted with a purely oscillatory ansatz. The residuals between the numerical modes and the Hilbert fits are reported in the bottom panels (gray). While the phase of the oscillations is well reproduced, there is a larger discrepancy for the amplitude. A similar, but less evident, discrepancy is observed also in the Schwarzschild case, as already discussed in the main text (cfr. with Fig. 3). This is a further indication that future works could try different closed-form representations for the QNM-rescaled amplitude $A_{\bar{h}}$. However, it should be also noted that the NR modes do not approach zero exponentially in the late ringdown, thus indicating that improvements might be needed on the numerical side too³. Moreover, note that the nonspinning configurations with $q = 2, 3$ have

unexpected behaviors before $t_{A_{22}}^{\text{peak}}$. Given these considerations, we decide to employ waveforms generated by the surrogate NRHybSur3dq8 [54], rather than using directly SXS waveforms. Therefore, for the comparable mass configurations, we select systems with $q \in [1, 8]$ and spins $\chi \in [-0.8, 0.8]$; for each (q, χ) -pair, we consider $(\chi_1, \chi_2) = \{(\chi, 0), (\chi, \chi), (0, \chi)\}$. Using the surrogate thus facilitates the location of waveforms in the parameter space, improving the quality of the hierarchical global fits. Alternative strategies to be investigated in the future include the computation of the Bondi mass aspect from CCE data by removing the displacement memory contribution using Eq. (3), mapping the SXS data to the superrest frame, or considering also data from different catalogs, such as the RIT one [128–131].

Finally, we also explored the amplitude ansatz introduced in Ref. [132], which reads

$$A_{\bar{h}} = \left(\frac{c_1^A}{1 + e^{-c_2^A \tau + c_3^A}} + c_4^A \right)^{\frac{1}{c_5^A}}. \quad (9)$$

We tested different combinations of constrained parameters, both constraining only two parameters using A_0 and \dot{A}_0 , and three parameters using \ddot{A}_0 too. While the fitted amplitude was more accurate for the test-mass primary fits, the global fits over the parameter space were not stable, in the sense that the argument of the c_5^A -root could become negative when reconstructed from the hierarchical fits. This problem seems to arise only when the fit of the multipole does not start from its own peak, *i.e.* when $\dot{A}_0 \neq 0$. While Eq. (9) was successfully employed to describe the (2,2) multipole in Refs. [106, 132], we find Eq. (4) to be more robust for the fits of the (2,0) mode.

Hierarchical global fits – Once that we have performed the primary fits on our dataset, we need to provide global fits for the fitted coefficients $\{c_2^A, c_3^A, c_2^\phi, c_3^\phi\}$ over the parameter space, together with the needed numerical quantities, $\{A_0, \dot{A}_0, \omega_0\}$. As explained in the

³ This slower decay could be linked to a physical power-law tail, but it may be also related to the residual drift of the center of mass observed in SXS simulations [127].



FIG. 6. Primary Hilbert fits of the (2,0) mode (dashed green) performed for different SXS configurations (black). Residuals in the bottom panels. The vertical bands mark the \mathcal{H} -fitting intervals. Note the different vertical scales.

main text, we start by performing a 1-dimensional fit over the test-mass simulations using a quadratic ansatz

$$f_{\nu=0}(\hat{a}) = b_0 + b_1\hat{a} + b_2\hat{a}^2, \quad (10)$$

where \hat{a} is the Kerr spin. The constant coefficient is fixed to be the Schwarzschild value. Following the discussion of the main text on the phenomenologies of the (2,0) mode, for A_0 and \dot{A}_0 we impose $b_1 = -b_0 - b_2$ in order to have $f_{\nu=0}(1) = 0$, and fit b_2 on the Kerr data. For the other quantities, we fit both b_1 and b_2 . Note that

for ω_0 we only employ data up to $\hat{a} = 0.6$ for this 1-dimensional fit, since higher-degree polynomials would be needed to capture its behavior over the whole spin range $\hat{a} \in [-1, 1]$ and, as already mentioned, the (2,0) mode is strongly suppressed for high positive spins. We then perform another 1-dimensional fit over ν for the non-spinning configurations,

$$f_{\hat{a}=0}(\nu) = b_0 + c_1\nu + c_2\nu^2. \quad (11)$$

We then combine these two fits in a 2-dimensional ansatz,

$$f_{2D}(\tilde{a}_0, \nu) = b_0 + b_1 \tilde{a}_0 + b_2 \tilde{a}_0^2 + (c_1 + d_{11} \tilde{a}_0 + d_{21} \tilde{a}_0^2) \nu + (c_2 + d_{12} \tilde{a}_0 + d_{22} \tilde{a}_0^2) \nu^2, \quad (12)$$

where we remind that $\tilde{a}_0 \equiv (\chi_1 m_1 + \chi_2 m_2)/M$ generalizes the Kerr spin \hat{a} , and the d_{ij} coefficients have to be determined from the data. For A_0 and \dot{A}_0 , we impose $d_{2j} = -c_j - d_{1j}$, so that $f_{2D}(1, \nu) = 0$, and we determine d_{1j} using the remaining simulations of our dataset. The same simulations are used to determine all the d_{ij} coefficients for the other fitted quantities. The coefficients found with this approach are reported in Table I for all the needed quantities.

NQC and ringdown matching – In order to achieve an IMR model, each multipole of the inspiral/plunge EOB waveform $h_{\ell m}^{\text{inspl}}$ has to be completed with a post-merger model $h_{\ell m}^{\text{rng}}$. The matching between the two waveforms is performed as

$$h_{\ell m} = h_{\ell m}^{\text{inspl}} \hat{h}_{\ell m}^{\text{NQC}} \theta(t_{\ell m}^{\text{match}} - t) + h_{\ell m}^{\text{rng}} \theta(t - t_{\ell m}^{\text{match}}), \quad (13)$$

where $\theta(t - t_{\ell m}^{\text{match}})$ is the Heaviside step-function, $t_{\ell m}^{\text{match}}$ is the matching time, and the NQC corrections $\hat{h}_{\ell m}^{\text{NQC}}$ ensures the continuity between the inspiral and ringdown waveforms. In state-of-the-art EOB models, the quasi-circular inspiral waveform $h_{\ell m}^{\text{inspl}}$ of the $m > 0$ modes is factorized and resummed according to Ref. [133]. Further resummation procedures for the residual PN amplitude and phase corrections have been explored during the years. However, in this work we focus on the $m = 0$ modes, and we only consider the formally Newtonian prescription outlined in Ref. [26], which yields Eq. (2) for the (2,0) mode. The NQC corrections are explicitly written as

$$\hat{h}_{\ell m}^{\text{NQC}} = \left(1 + \sum_{i=1}^3 a_i^{\ell m} n_i \right) \exp \left(i \sum_{j=1}^3 b_j^{\ell m} n_{j+3} \right), \quad (14)$$

where n_i are functions written in terms of time-derivatives of the radius and in terms of the conjugate momentum of the tortoise coordinate $p_{r_*} \equiv \sqrt{A/B} p_r$, where A and B are the EOB metric potentials; see, *e.g.*, Ref. [134] for more details. A common choice for the higher modes is

$$n_1 = \frac{p_{r_*}^2}{r^2 \Omega^2}, \quad (15a)$$

$$n_2 = \frac{\ddot{r}}{r \Omega^2}, \quad (15b)$$

$$n_3 = n_1 p_{r_*}^2, \quad (15c)$$

$$n_4 = \frac{p_{r_*}}{r \Omega}, \quad (15d)$$

$$n_5 = n_4 \Omega, \quad (15e)$$

$$n_6 = n_5 p_{r_*}^2, \quad (15f)$$

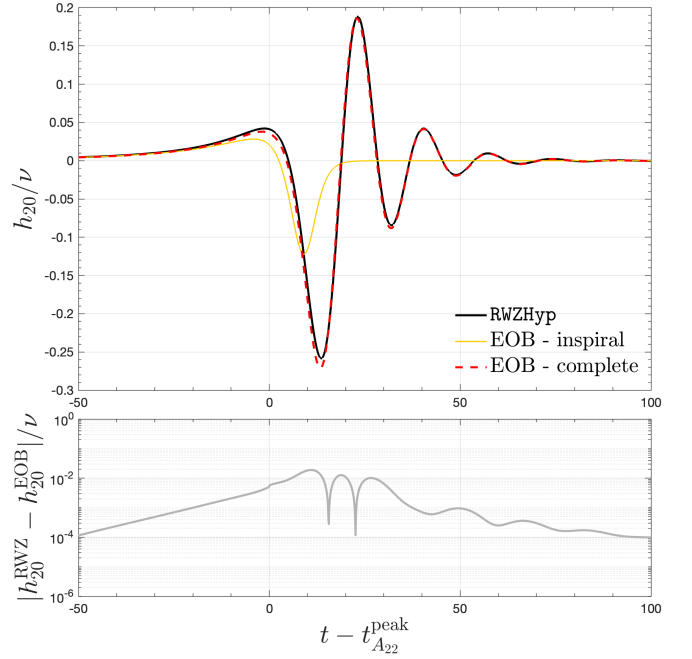


FIG. 7. Comparison between the numerical and complete EOB waveform for the Schwarzschild case (black and dashed red, respectively). We also show the EOB inspiral waveform h_{20}^{inspl} (solid yellow). The residual is reported in bottom panel.

where Ω is the orbital frequency. The coefficients a_i and b_j of Eq. (14) are determined by solving, in general, the following linear system

$$A_{\ell m}^{\text{EOB}}(t_{\ell m}^{\text{NQC}}) = A_{\ell m}^{\text{rng}}(t_{\ell m}^{\text{NQC}}), \quad (16a)$$

$$\dot{A}_{\ell m}^{\text{EOB}}(t_{\ell m}^{\text{NQC}}) = \dot{A}_{\ell m}^{\text{rng}}(t_{\ell m}^{\text{NQC}}), \quad (16b)$$

$$\ddot{A}_{\ell m}^{\text{EOB}}(t_{\ell m}^{\text{NQC}}) = \ddot{A}_{\ell m}^{\text{rng}}(t_{\ell m}^{\text{NQC}}), \quad (16c)$$

$$\omega_{\ell m}^{\text{EOB}}(t_{\ell m}^{\text{NQC}}) = \omega_{\ell m}^{\text{rng}}(t_{\ell m}^{\text{NQC}}), \quad (16d)$$

$$\dot{\omega}_{\ell m}^{\text{EOB}}(t_{\ell m}^{\text{NQC}}) = \dot{\omega}_{\ell m}^{\text{rng}}(t_{\ell m}^{\text{NQC}}), \quad (16e)$$

$$\ddot{\omega}_{\ell m}^{\text{EOB}}(t_{\ell m}^{\text{NQC}}) = \ddot{\omega}_{\ell m}^{\text{rng}}(t_{\ell m}^{\text{NQC}}). \quad (16f)$$

In this work we do not consider second-order derivatives for the (2,0) mode, and therefore include only $\{n_1, n_2, n_4, n_5\}$ in the NQC base. The quantities on the left-hand-side are evaluated from $h_{\ell m}^{\text{inspl}} \hat{h}_{\ell m}^{\text{NQC}}$, while the right-hand-side is computed from the ringdown waveform. Note that the coefficients are found by solving the system (16) at a specific time, $t_{\ell m}^{\text{NQC}}$, but the NQC corrections are applied on an extended time interval. Therefore, phase and amplitude should be ideally monotonic up to the matching time for optimal results.

By complexifying the oscillatory contribution of the (2,0) mode (or any other $m = 0$ mode) via a Hilbert transform, we obtain amplitudes and phases that are qualitatively similar to the ones of the $m > 0$ modes, and we can thus apply the NQC corrections to match the complexified inspiral (2,0) waveform with the post-merger Hilbert model. We report in Fig. 7 the result

TABLE I. Coefficients of the hierarchical global fits performed with the ansatz of Eq. (12) over the test-mass simulations listed in Table II and waveforms generated with NRHybSur3dq8.

	b_0	b_1	b_2	c_1	c_2	d_{11}	d_{21}	d_{12}	d_{22}
A_0	0.07647	-0.13512	0.05865	-0.19955	0.33426	0.37027	-0.17072	-0.20921	-0.12505
\dot{A}_0	0.00786	-0.01705	0.00919	-0.02534	0.02541	0.05440	-0.02905	-0.01746	-0.00795
ω_0	0.08950	-0.02150	-0.00671	0.13470	-0.03056	-0.02966	-0.21276	-0.07630	0.71567
c_2^A	0.13295	-0.01104	-0.02368	-0.08291	1.30014	0.11119	0.48070	0.61649	-1.69515
c_3^A	-1.61888	-0.20029	-0.08509	2.52896	2.43339	3.61367	2.34373	-10.88689	-6.28732
c_2^ϕ	0.15313	0.00082	-0.01702	-0.04679	1.23738	-0.08273	-0.01566	0.61189	-0.03258
c_3^ϕ	4.41377	6.15871	5.23689	-23.3638	240.998	-45.5214	-33.2851	347.687	185.324

of this matching for the Schwarzschild case, where we used the most natural choice $t_{20}^{\text{NQC}} = t_{A_{22}}^{\text{peak}}$, which we tested to work well also for the Kerr cases. Note that the value of the EOB waveform at the matching time is not equal to the numerical one, despite the hierarchical fits exactly incorporating the Schwarzschild limit. This is due to the fact that when the matching is performed, we rotate the complex ringdown signal of a certain phase determined by the inspiral/plunge waveform. We thus lose the aforementioned property, which is instead observed in the primary fits. For generic mass ratios, we find that the choice $t_{20}^{\text{NQC}} = t_{A_{22}}^{\text{peak}} - 2$ yields a better numerical/analytical agreement. In these cases, the right-hand-side of Eqs. (16) is still evaluated from the post-merger waveform, which is extrapolated back in time up to t_{20}^{NQC} . Finally, since we determine a_i and b_j at $t_{20}^{\text{NQC}} = t_{A_{22}}^{\text{peak}} - 2$ but still perform the match at $t_{A_{22}}^{\text{peak}}$,

a small discontinuity would be observed at the matching time. This can be easily cured with a cubic patch applied between $t_{20}^{\text{NQC}} - 1$ and $t_{A_{22}}^{\text{peak}} + 4$. The four coefficients of the patch are determined by requiring C_1 -continuity conditions at both ends. Note that this second patch is applied on the real physical mode after matching. This patch ensures a continue and reliable waveform, as shown from the EOB/NR comparisons reported in Fig. 4 and 8.

Low-frequency PN-matching for null memory

– Since we start our EOB evolution at finite radius and compute the (2,0) memory contribution from the corresponding fluxes through Eq. (3), we have $h_{20}^{\text{memo}} \neq 0$ for $\Omega \rightarrow 0$. To cure this unphysical property, the result from Eq. (3) can be matched to the PN analytical formula, which has the correct low-frequency behavior. We perform the matching with the 3.5PN nonspinning result [75, 76] plus the 1.5PN spinning contribution [93]. The complete expression thus reads

$$\begin{aligned}
h_{20}^{\text{memo}, 3.5\text{PN}} = & \frac{4}{7} \sqrt{\frac{5\pi}{6}} \nu x \left\{ 1 + \left(-\frac{4075}{4032} + \frac{67}{48} \nu \right) x + \left(\frac{-2813 + 756\nu}{2400} \tilde{a}_0 + \frac{3187}{2400} \delta \chi_A \right) x^{3/2} + \right. \\
& \left(-\frac{151877213}{67060224} - \frac{123815}{44352} \nu + \frac{205}{352} \nu^2 \right) x^2 + \pi \left(-\frac{253}{336} + \frac{253}{84} \nu \right) x^{5/2} + \\
& \left[-\frac{4397711103307}{532580106240} + \left(\frac{700464542023}{13948526592} - \frac{205}{96} \pi^2 \right) \nu + \frac{69527951}{166053888} \nu^2 + \frac{1321981}{5930496} \nu^3 \right] x^3 \\
& \left. \pi \left(\frac{38351671}{28740096} - \frac{3486041}{598752} \nu - \frac{652889}{598752} \nu^2 \right) x^{7/2} \right\} \quad (17)
\end{aligned}$$

where $\delta = (m_1 - m_2)/M$, $\chi_A = (m_1 \chi_1 - m_2 \chi_2)/M$, and $x = \Omega^2/3$. We then compute the residual between the memory contribution obtained from the radiated energy flux and the 3.5PN expression, which is then fitted with the ansatz $\text{Res}(x) = d_0 + d_5 x^5 + d_{5.5} x^{11/2}$ for $t < t_{\text{end}}^{\text{fit}}$, where $t_{\text{end}}^{\text{fit}} = t_{A_{22}}^{\text{peak}} - 500$. For the non spinning equal mass case, this time corresponds to $x \sim 0.105$. The coefficient d_0 is then added to the result obtained from

Eq. (3), so that $h_{20}^{\text{memo}} \rightarrow 0$ for $t \rightarrow -\infty$. Note that a similar approach has been followed in Ref. [94], but with different choices for the amount of analytical PN information employed and, consequently, for the fitting ansatz of the residual. We tested that choosing different time intervals for the fit of the residual does not significantly influence d_0 . Similarly, using less analytical information or more free coefficients in the ansatz yield equivalent re-

sults. However, the PN series does not typically converge in strong field regimes, therefore one should be careful in choosing $t_{\text{end}}^{\text{fit}}$ too close to the merger time.

EOB/NR unfaithfulness – To assess the accuracy of the model more systematically across the parameter space, we consider frequency-domain mismatches between the full EOB and NR (2,0) multipoles. We compute the mismatch (or *unfaithfulness*) between two signals as

$$\bar{\mathcal{F}} = 1 - \max_{t_0, \phi_0} \frac{\langle h_1, h_2 \rangle}{\langle h_1, h_1 \rangle \langle h_2, h_2 \rangle}, \quad (18)$$

where

$$\langle h_i, h_j \rangle = 4\Re \int_{f_{\min}}^{f_{\max}} \frac{\tilde{h}_i \tilde{h}_j^*}{S_n(f)} df, \quad (19)$$

and \tilde{h}_i is the Fourier transform of h_i , while $S_n(f)$ is the zero-detuned, high-power noise spectral density of Advanced LIGO [121]. We make use of the package `pycbc` [135]. With this noise, mismatches are usually computed in the frequency range $[f_{\min}, f_{\max}] = [10, 1024]$ Hz, which we also consider in this work. Therefore, our computation mainly tests the accuracy of the oscillatory contribution of the waveform, which is the main novelty of this work. The memory, which is a low-frequency component, marginally influences this computation. Moreover, since the computation involves a numerical fast Fourier transform, ensuring periodicity is crucial to prevent spectral leakage. To address this in the case of signals with displacement memory, recent studies have explored different methodologies [136, 137]. In this work,

we employ a time-domain windowing technique similar to that discussed in Sec. IV E.1 of Ref. [136].

Mismatches calculated using only the (2,0) modes for binaries with mass ratio up to $q = 8$ and different spins configurations with $\chi_i \in [-0.8, 0.8]$ are reported in the right panel of Fig. 4 and discussed in the main text.

Finally, when considering more multipoles as in the case of the non-spinning equal-mass quadrupolar waveforms discussed in the conclusions, we consider the sky-maximized overlap statistic [138]. We have verified that, for current detections, the impact of the (2,0) mode on the mismatch of the $\ell = 2$ quadrupolar waveforms is negligible.

Additional time-domain comparisons – We report in Fig. 8 some additional time-domain EOB/NR comparisons between the complete (2,0) obtained with the method outlined in this work by using `TEOBResumS-GIOTTO` as a baseline and the (2,0) mode of the surrogate model `NRHybSur3dq8_CCE`. Visually, the main source of disagreement between the two model is given by the different final offset, while the oscillatory parts are more similar. Considering that the offset of the modes is consistent before merger, and considering that for the equal mass nonspinning case the final offset is essentially the same (cfr. with Fig. 4), we are prone to think that the source of this disagreement has to be searched in the amplitude of the higher modes with $m > 0$ during the merger-ringdown phase, as already argued in the main text. The improvement of these modes is beyond the scope of this work, and we thus defer this investigation.

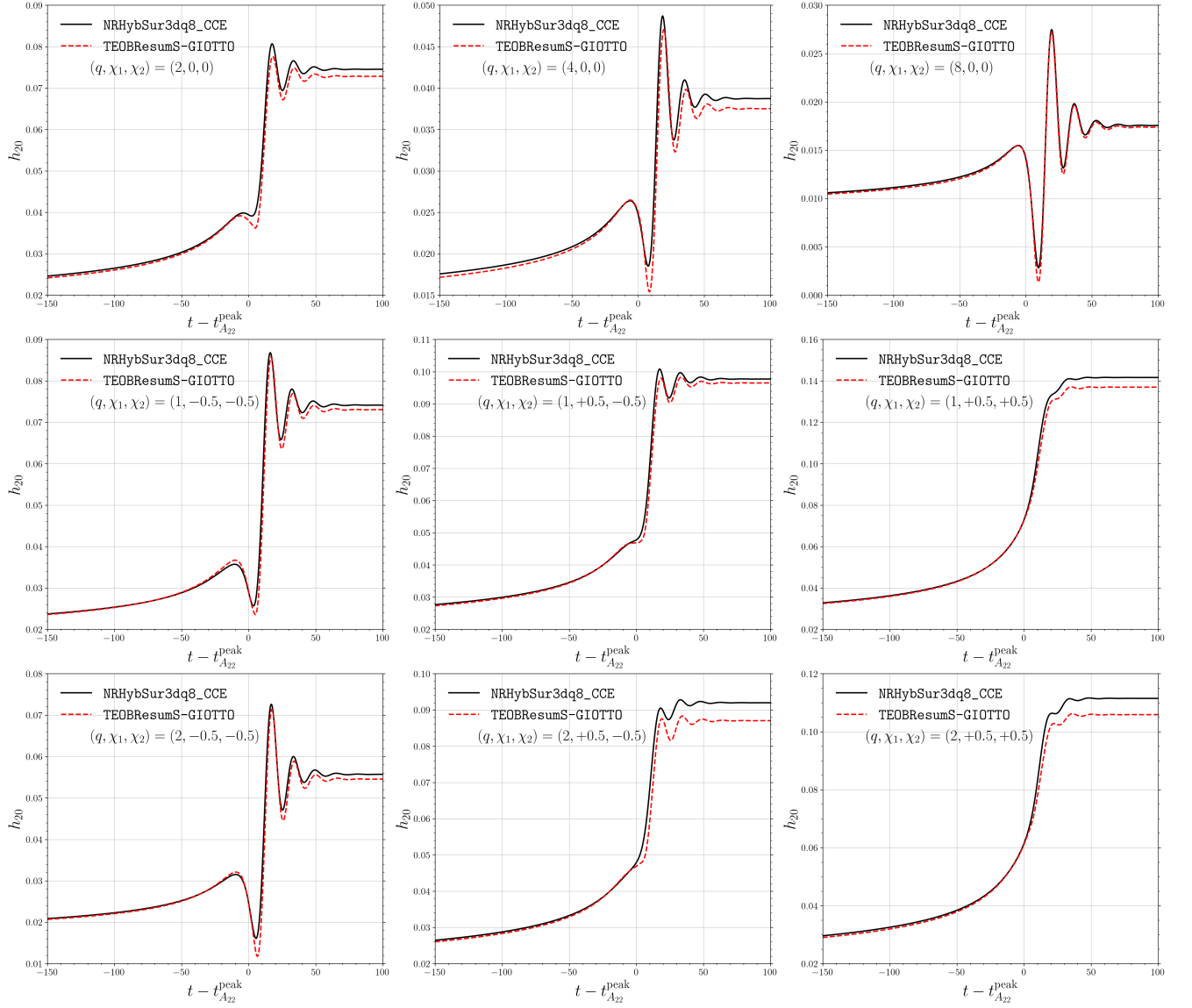


FIG. 8. Comparisons of $(2,0)$ modes for comparable mass configurations. We consider the modes from NRHybSur3dq8_CCE and the ones computed in this work using TEOBResumS-GIOTTO as a baseline.

TABLE II. Quasi-circular test-mass simulations considered in this work. We considered $\nu = 10^{-3}$ in the dissipative part of the dynamics, but no ν -corrections have been included in the Schwarzschild and Kerr Hamiltonians.

code	\hat{a}	r_0	A_0	\dot{A}_0	ω_0	c_2^A	c_3^A	c_2^ϕ	c_3^ϕ
Teukode	-0.90	9.35	0.2456169	0.0310443	0.1041740	0.12475	-1.48859	0.14000	2.70793
Teukode	-0.60	8.55	0.1776497	0.0212031	0.0995899	0.13025	-1.54394	0.14473	2.79897
Teukode	-0.50	8.25	0.1575544	0.0184084	0.0978831	0.13173	-1.55649	0.14782	3.03224
Teukode	-0.30	7.70	0.1222918	0.0136646	0.0950989	0.13344	-1.57392	0.15165	3.47555
RWZHyp	0.00	7.00	0.0764704	0.0078630	0.0895022	0.13295	-1.61888	0.15313	4.41377
Teukode	0.30	5.90	0.0419396	0.0038958	0.0852170	0.12913	-1.64958	0.15469	6.06861
Teukode	0.50	5.25	0.0225565	0.0018838	0.0779949	0.12231	-1.72724	0.15075	8.51613
Teukode	0.60	4.90	0.0145450	0.0011256	0.0720827	0.11605	-1.80273	0.14477	10.69553
Teukode	0.70	4.50	0.0080635	0.0005633	0.0640581
Teukode	0.80	4.10	0.0032148	0.0001903	0.0507208
Teukode	0.90	3.55	0.0004914	0.0000202	0.0267972
Teukode	0.95	3.20	0.0000337	0.0000008	0.0074474